



Chemical vs thermal exfoliation of g-C₃N₄ for NO_x removal under visible light irradiation

Ilias Papailias^{a,b}, Nadia Todorova^{a,*}, Tatiana Giannakopoulou^a, Nikolaos Ioannidis^a, Nikos Boukos^a, Chrysoula P. Athanasekou^a, Dimitra Dimotikali^b, Christos Trapalis^{a,*}

^a Institute of Nanoscience and Nanotechnology, NCSR “Demokritos”, Athens, 15341, Greece

^b Department of Chemical Engineering, National Technical University of Athens, Athens, 15780, Greece

ARTICLE INFO

Keywords:

g-C₃N₄
Exfoliation
NO_x
Visible light
EPR

ABSTRACT

Graphitic carbon nitride (g-C₃N₄) has emerged as one of the most promising visible light active photocatalysts for NO_x removal. Due to its low efficiency in bulk form though, many methods have been applied in order to improve the optical properties and photocatalytic activity. Among them, exfoliation via chemical and thermal treatment appears to be very effective and easy to perform. In this work, g-C₃N₄ was exfoliated by high-yield chemical and thermal treatment. A thorough comparative investigation was performed, revealing successful exfoliation of g-C₃N₄ and significantly enhanced visible light photocatalytic activity. Both methods led to high pore volume and specific surface area. It was established that chemical exfoliation resulted in wider band gap with more positive VB edge in comparison to thermal exfoliation. Furthermore, increased superoxide radical formation and reactivity of photogenerated electrons was demonstrated by EPR measurements in the case of chemical exfoliation. The chemically exfoliated g-C₃N₄ showed superior photocatalytic performance in NO_x removal under visible light irradiation. This outcome was ascribed to the increased superoxide radical formation, the favorable band gap edges and porosity of the materials.

1. Introduction

In recent years, the uncontrolled usage of fossil fuels has given rise to multiple environmental problems. Among them, the increasing concentration of nitrogen oxides (NO_x) in the air has been recognized as one of the most serious, as it is considered responsible for acid rain, photochemical smog and haze [1]. Especially in populated cities, NO_x also constitute a serious health hazard for the human respiratory system [2]. Therefore, the development of efficient methods to promote the NO_x removal from the atmosphere is becoming increasingly important. Among the methods that have been applied, heterogeneous photocatalysis is considered a very promising solution to the problem due to the utilization of solar light, the low cost and the potential of large scale implementation.

Many photocatalysts have been explored to date, including metal-containing and metal-free semiconductors [3,4]. Among them, g-C₃N₄ has drawn significant attention due to its thermal and chemical stability, moderate band gap (~2.7 eV) and facile preparation [5,6]. These properties make g-C₃N₄ a promising material for various applications, such as environmental remediation, hydrogen or oxygen evolution,

carbon dioxide reduction, lithium batteries and supercapacitors [7–10]. However, bulk g-C₃N₄ has large particle size and suffers from low specific surface area as well as high recombination rate of the photo-generated electron-hole pairs, which results in low photocatalytic activity and limited performance. In order to improve the activity of g-C₃N₄ many methods have been employed, such as doping [11], metal-deposition [12], creation of vacancy defects [13,14] and preparation of heterojunctions with CdS [15], Bi₂WO₆ [16], TiO₂ [17], MoS₂ [18] etc. Although these strategies are quite effective, a more simple and economic approach is required for large scale applications. In this direction, the exfoliation of g-C₃N₄ appears as an easy and beneficial method for enhancing its photocatalytic efficiency.

Currently, a number of relative research articles on chemical and thermal treatment of g-C₃N₄ have been published. Xu et al. prepared single atomic layer g-C₃N₄ by a simple chemical exfoliation method [19]. Tong et al. demonstrated that g-C₃N₄ could be rapidly disintegrated and exfoliated in concentrated H₂SO₄ when water is added [20]. Li et al. reported a facile method to prepare dispersible g-C₃N₄ by chemical oxidation at room temperature [21]. Niu et al. synthesized g-C₃N₄ thin layers via thermal-oxidation by etching dicyandiamide-

* Corresponding authors.

E-mail addresses: n.todorova@inn.demokritos.gr (N. Todorova), c.trapalis@inn.demokritos.gr (C. Trapalis).

<https://doi.org/10.1016/j.apcatb.2018.07.078>

Received 25 May 2018; Received in revised form 26 July 2018; Accepted 30 July 2018

Available online 31 July 2018

0926-3373/ © 2018 Elsevier B.V. All rights reserved.

derived bulk g-C₃N₄ in air [22]. Dong et al. treated thiourea-derived bulk g-C₃N₄ in air under different temperatures [23]. Li et al. developed a simple thermal oxidation method for preparing different g-C₃N₄ nanostructures, by controlling the process temperature and time [24].

In the present study, g-C₃N₄ was exfoliated by high-yield chemical and thermal treatment, in order to achieve enhanced photocatalytic activity. The novel materials were characterized and measured for NO oxidation under visible light irradiation. For the first time, a side-by-side comparison of the two methods is presented where their advantages and disadvantages are discussed.

2. Experimental

2.1. Sample preparation

All chemicals were of analytical grade and were used without any further purification. Melamine powder was purchased from Alfa Aesar. Sulfuric acid (H₂SO₄, 98%) was purchased from Chem-Lab and isopropanol (IPA) from Sigma-Aldrich. The spin trap 5,5-dimethyl-1-pyrroline N-oxide (DMPO) was purchased from Sigma-Aldrich and 2,2,6,6-tetramethylpiperidine-1-oxyl (TEMPO) was purchased from Alfa Aesar.

Initially, bulk g-C₃N₄ was synthesized by thermal polycondensation of melamine. In detail, 4 g of melamine was put into an open alumina crucible and heated in a tube furnace to 550°C with a rate of 20°C/min and remained there for 3 h. Argon flow was used in all experiments in order to achieve inert atmosphere. The yellow product was collected and ground into powder, while the final yield was 0.8 g. This sample was named Bulk.

2.1.1. Chemical treatment

For the chemical treatment, 0.5 g of Bulk g-C₃N₄ was stirred in 8 mL concentrated H₂SO₄ for 1 h, 3 h and 5 h. Then 2 mL distilled H₂O was added slowly under stirring, during which the temperature increased rapidly due to the exothermic process. The resulting suspension was poured into 100 mL distilled H₂O and washed several times with distilled water until pH 7 was achieved. The remaining white powder was re-dispersed into 100 mL IPA and ultrasonicated for 1 h. The suspension was dried overnight at 60°C and the final yield was 0.32 g in all cases. The samples obtained were named Chem1, Chem3 and Chem5 with regard to the treatment time.

2.1.2. Thermal treatment

For the thermal treatment, 0.5 g of Bulk g-C₃N₄ was added in an open alumina crucible and placed in a tube furnace with both sides open in order to achieve free air flow. The powder was heated at 550°C for 1 h, 2 h and 3 h and the final yield was 0.72 g, 0.40 g and 0.15 g, respectively. This weight loss is ascribed to the decomposition of g-C₃N₄ to gaseous products during thermal treatment. Interestingly, the volume of the powders increased with the extended treatment time (Fig. S1) and the color also varied from intense to pale yellow, respectively. The samples obtained were named Ther1, Ther2 and Ther3.

2.2. Characterization

A Siemens D500 X-Ray diffractometer with a Cu K α radiation source was used for the XRD measurements. SEM characterization was performed using a FEI Quanta Inspect Microscope equipped with tungsten filament operating at 25 kV and an EDS detector. TEM analysis was performed to examine the morphology of the materials utilizing a FEI CM20 TEM. The N₂ adsorption-desorption isotherms were obtained with a Quantachrome Autosorb-iQ instrument. Elemental analysis was performed with a PerkinElmer 2400 CHN analyzer. The FT-IR transmittance spectra of the materials embedded in KBr pellets were measured on a Perkin Elmer Spectrum BX instrument. X-Ray photoelectron spectroscopy was conducted with ultrahigh vacuum VG EXCALAB 210 electron spectrometer using Mg K α (1253.6 eV) as radiation source. The

UV-vis diffuse reflectance spectra were recorded by a Shimadzu UV-2100 spectrophotometer using BaSO₄ as reference.

2.3. Electrochemical measurements

The conduction band edge potential of the investigated materials was determined using the Mott-Schottky (MS) approximation [25] by plotting the inverse square of space charge capacitance (1/C²) against the applied potential and taking the intercept of the plot linear part with the potential axis. The measurements were performed using the Electrochemical Impedance Spectroscopy (EIS) on a Metrohm Autolab PGSTAT302 potentiometer equipped with a beaker-type three-electrode cell. Glassy carbon (GC) electrode, Pt sheet and Ag/AgCl KCl (3 M) electrode were used as the working, counter and reference electrodes, respectively. The working electrode materials were prepared in a typical way described in our recent work [26]. For the measurements, 0.1 M KCl aqueous solution was used as electrolyte. The impedance data at five frequencies, specifically at 10, 31, 100, 316 and 1000 Hz were measured for different potential values that varied from −1.2 V to 0.5 V. The imaginary part of the measured impedances provided the space charge capacitance values [27]. Then, the MS plots at each frequency were constructed from the collected data as a function of the applied potential.

2.4. EPR spectroscopy

The EPR measurements were obtained with an extensively upgraded Bruker ER-200D spectrometer interfaced to a personal computer and equipped with an Oxford ESR 900 cryostat, an Anritsu MF76 A frequency counter and a Bruker 035 M NMR gauss meter. The perpendicular 4102ST cavity was used and the microwave frequency was 9.41 GHz. All room temperature EPR measurements were carried out with the following settings to detect the spin adducts: 20 mW microwave power, 8 mT scan range and 1 Gpp field modulation.

The formation of reactive oxygen species (ROS) under visible light irradiation by the prepared g-C₃N₄ materials was investigated by employing a method for scavenging the short lived ROS. This was achieved by allowing them to react with the nitron DMPO which is a spin trap. The spin trap is an EPR silent species which can form an adduct with a ROS by transferring an electron to it. DMPO is a convenient spin trap used in photochemical systems due to its low photoactivity, wide potential window and solubility in polar and non-polar solvents. The products of these reactions are temporally more persistent nitroxide spin adducts, which themselves are paramagnetic (Fig. S2). These adducts can then be measured and identified by EPR spectroscopy [28,29]. The samples were suspended in acetonitrile at a concentration of 0.25 mg/mL. DMPO was added to a final concentration of 0.1 M prior to 80 s visible light irradiation. At least 50 μ L aliquots of bulk or exfoliated g-C₃N₄ suspensions were placed in open ended capillary tubes with internal diameter of 0.9 mm which were then sealed at one end. The capillary tubes were inserted into 4 mm EPR tubes and placed into the EPR cavity, where the spectra were recorded. Visible light irradiation was applied outside the EPR cavity, prior to measurements, for various time intervals using a 360 W/82 V tungsten lamp. After irradiation, the samples were gently purged with N₂ for 30 s in order to substantially decrease the concentration of dissolved O₂. The latter, due to its paramagnetism, caused line broadening to the EPR spectra of radical adducts with spin traps. The experimental isotropic EPR spectra were analyzed and simulated using the EasySpin-5.0.2 software package [30]. Hyperfine coupling constants for aqueous ROS adducts with DMPO in acetonitrile were taken from the literature [31].

The reactivity of electrons generated by visible light irradiation towards the spin label TEMPO (a stable organic radical) was studied by EPR spectroscopy. For this experiment, the EPR signal intensity of TEMPO 0.05 mM upon irradiation time was measured, in the presence of 0.4 mg/mL g-C₃N₄ samples suspended in acetonitrile containing 20%

v/v DMSO. Upon visible light irradiation, electrons from the VB are excited to the CB, creating positively charged holes. TEMPO is a typical spin label molecule that can be reduced by these electrons to give a hydroxyl amine, TEMPOH, which is EPR silent (Fig. S3). DMSO acts as a hole scavenger added to inhibit the charge recombination.

2.5. Photocatalytic activity evaluation

The photocatalytic activity of the materials in air purification was evaluated using a standard procedure based on ISO/DIS 22197-1 [32]. According to the standard and relevant scientific papers [33–35], NO gas is adsorbed on the surface of the photocatalysts and oxidized to NO₂ gas followed by oxidation to nonvolatile NO₃[−] under irradiation. In the case of g-C₃N₄ photocatalysts, DRIFT and DFT studies suggest that nitrogen atoms are the preferred oxidation sites while carbon atoms provide the reduction sites [5,36,37].

In our experiments the samples were prepared by pressing the photocatalytic materials in flat holders with surface area of 20 cm², which were then placed in a continuous flow reactor with dimensions 30 cm x 5 cm. The relative humidity (RH) was set to 50% as required by the standard. In order to achieve that, dry air of 1.5 L/min and wet air of 1.5 L/min were set by Bronkhorst EL-FLOW mass flow controllers, to a total air flow of 3 L/min (equivalent to a velocity of approximately 0.2 m/s). The relative humidity inside the reactor was measured by a HANNA HI-9565 Thermo-Hygrometer with an accuracy of ± 3% RH. The NO gas was supplied from a compressed (50 ppm) gas cylinder Linde Hellas Ltd. Its concentration in the reactor was set to 1 ppm by applying a flow rate of 60 mL/min. The gas stream ran over each sample in the dark for a period of 5 min, to reach equilibrium between the sample and the gas phase at 1 ppm.

The photocatalytic activity of the materials was measured under visible light irradiation (Nordex T5-8W-4000 K lamps) with intensity of 7000 lx for 30 min at ambient temperature. The concentrations of NO, NO₂ and NO_x (where NO_x represents the sum of NO and NO₂) were monitored using a Horiba APNA-370 chemiluminescence-based NO_x analyzer (with lower detectable limit of 0.0005 ppm) equipped with an O₃ lamp and a silicon photodiode sensor. A schematic illustration of the experimental setup is presented in Fig. S4. The materials showed reproducible photocatalytic activity, which was tested using three samples of each material.

3. Results and discussion

3.1. Crystalline structure

The XRD patterns of bulk and exfoliated g-C₃N₄ are presented in Fig. 1. For Bulk sample, the two characteristic peaks of g-C₃N₄ are observed. Namely, the weak peak at 13.1° corresponds to the (100)

plane, which is related to the in-plane structural packing motif of tri-s-triazine units with an interplanar distance of $d = 0.675$ nm [38,39]. The strong diffraction peak at 27.5° corresponds to the (002) plane, which is attributed to the interlayer stacking of aromatic rings with a distance of $d = 0.324$ nm [40,41]. Lower crystallinity and loose interlayer structure is observed after chemical and thermal treatment. Specifically, the intensity of the (100) and (002) peaks decreases indicating smaller planar size and lower number of aligned layers, respectively. Both types of changes are more prominent for the chemically treated g-C₃N₄. In fact, the (100) peak is completely absent from the patterns of samples Chem3 and Chem5, indicating a significant reduction of layers' size as a result of the intense H₂SO₄ treatment. The reduced intensity of (002) peak can be related to the delamination and increased layer disorder, demonstrating the achieved exfoliation of g-C₃N₄. Also, a defined shift of the (002) peak to larger diffraction angles is observed with the increase of the process time, indicating a denser packing due to the undulated layers gradually planarized during the process [42]. Thus, the calculated interlayer distance decreased gradually reaching the value of $d = 0.318$ nm for sample Chem5 (Table 1).

3.2. Surface area and morphology

The N₂ adsorption-desorption isotherms and the pore size distribution of the prepared materials are shown in Fig. 2. All materials showed characteristic hysteresis loops of type IV isotherms, which are typical for mesoporous materials [43]. The BET specific surface area (SSA) increased significantly after treatment. Interestingly, the thermally exfoliated g-C₃N₄ showed an increasing SSA depending on the treatment time (up to 127.63 m²/g), while the chemically exfoliated samples reached more than twelve times higher SSA (up to 134.42 m²/g) in comparison with Bulk regardless of the duration. Similarly, the total pore volume (V_p) increased after treatment. The small mesopores, indicated by the sharp peak at ~2 nm, can be assigned to the porosity within the g-C₃N₄ sheets. The large mesopores, observed as a wide peak at 3–40 nm can be ascribed to the pores formed between packed layers [44]. The thermal exfoliation seems to preserve the type of porosity, as both types of pores increase proportionally retaining the ratio between them. However, large pores with peak centered at ~12 nm prevail and appear as the majority after chemical exfoliation. This could be attributed to the rapid exothermic effect when water was added to the H₂SO₄, causing initial delamination of g-C₃N₄ [45]. The obtained high SSA and V_p are expected to enhance the number of active sites and accelerate the transfer of the pollutants and final products [46].

The SEM analysis also revealed significant differences in the morphology of the materials (Fig. 3). Bulk g-C₃N₄ exhibits a nonporous architecture of aggregated flakes, which explains the very low SSA of 9.64 m²/g. After chemical treatment, the materials showed a three-dimensional sponge-like framework with an interconnected porous

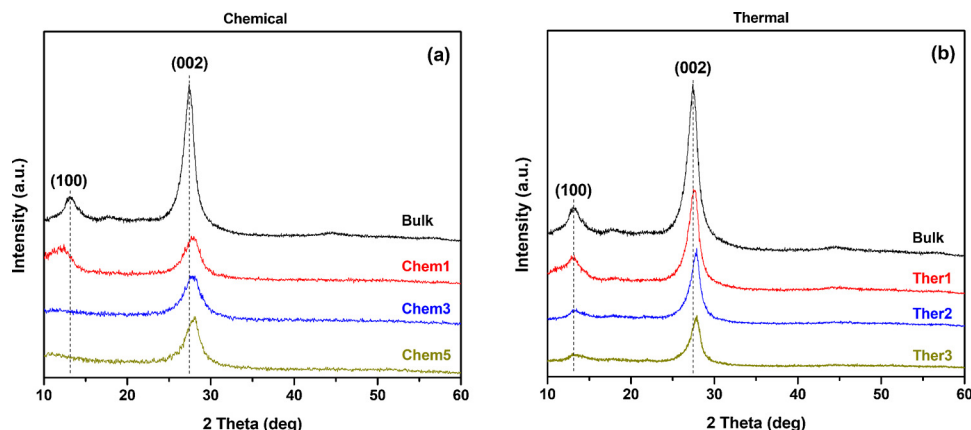


Fig. 1. XRD patterns of chemically (a) and thermally (b) exfoliated g-C₃N₄.

Table 1Interlayer distance (d), specific surface area (SSA), total pore volume (V_p), band gap energy (E_g), C/N atomic ratio and composition of the g- C_3N_4 materials.

Sample	(002) peak	d ^a (nm)	SSA (m ² /g)	V_p (cm ³ /g)	E_g (eV)	C/N	Composition ^b (%)		
							C	N	H
Bulk	27.5	0.324	9.64	0.050	2.63	0.635	35.25	64.66	1.14
Chem1	27.8	0.321	119.08	0.699	2.96	0.658	31.81	56.37	2.34
Chem3	27.8	0.321	134.42	0.856	2.97	0.662	32.14	56.59	2.33
Chem5	28.0	0.318	127.37	0.842	2.95	0.669	32.09	55.90	2.43
Ther1	27.6	0.323	21.20	0.140	2.65	0.630	34.02	62.96	0.69
Ther2	27.6	0.323	63.93	0.410	2.67	0.633	34.20	63.00	0.99
Ther3	27.8	0.321	127.53	0.799	2.72	0.634	34.19	62.59	1.30

^a Calculated through Bragg's law.^b Measured by elemental analysis.

structure, probably due to the H_2SO_4 intercalation and etching effect [47]. On the other hand, thermal treatment resulted in a sheet-like structure, in which the layers became thinner and more detached as the process time increased. The TEM analysis demonstrated that the treated g- C_3N_4 samples have few-layer structure typical for 2D exfoliated materials (Fig. 4). It can be observed that the chemically exfoliated g- C_3N_4 consists of layers with lower thickness than the thermally exfoliated g- C_3N_4 . These findings are in agreement with the BET and XRD results and indicate that a significant increase of interfacial contact between the air pollutant and the solid photocatalyst can be expected.

3.3. Chemical composition

The FT-IR analysis results are shown in Fig. 5. In general, the known characteristic peaks of g- C_3N_4 are observed. The broad peak at $3500\text{--}3000\text{ cm}^{-1}$ region corresponds to the adsorbed H_2O and N–H stretching from residual amino groups [43,48], while the absorption band at 884 cm^{-1} is associated with the cross-linking N–H deformation mode from these groups [49]. The sharp absorption peak at 805 cm^{-1} is attributed to the breathing mode of triazine units [50], while the peaks in the region from $1232\text{ to }1629\text{ cm}^{-1}$ correspond to the characteristic stretching of C–N heterocycles including trigonal N–(C)₃ and bridging H–N–(C)₂ units [51]. Compared to the Bulk g- C_3N_4 , there are some interesting changes in the spectra of the exfoliated materials. After chemical treatment, the intensity of the peaks at $1629\text{ and }1538\text{ cm}^{-1}$ decreased, while a peak at 1602 cm^{-1} appeared. This can be assigned to the structure of dimelem [52,53], indicating the cleavage of the bridging bond between tri-s-triazine units and the separation of the g- C_3N_4 network into smaller units [20,21]. These structural changes are also expressed by the decrease of the cross-linking N–H deformation mode at 884 cm^{-1} . Furthermore, peaks linked to oxygen containing groups at $963\text{ and }1082\text{ cm}^{-1}$ became more prominent, as a result of the hydrolysis/oxidation of g- C_3N_4 during the chemical treatment [20,54].

The thermally exfoliated materials showed similar peak features with Bulk g- C_3N_4 . However, the peaks showed increased intensity which can be attributed to the better arrangement and more ordered packing of tri-s-triazine units in the nanosheets [23,24].

The surface chemical composition of the prepared materials was investigated with XPS analysis and the obtained N1s and O1s spectra are shown in Fig. 6. The N1s spectra were deconvoluted into three peaks at 398.6, 400.3 and 401.4 eV, that can be assigned to sp^2 hybridized N in triazine rings (C=N–C), sp^3 hybridized tertiary N (in N–(C)₃ or H–N–(C)₂ groups) and residual amino functional groups (C–NHx), respectively [21,55]. The O1s spectra of Bulk and thermally exfoliated g- C_3N_4 revealed only one major peak at 532.4 eV, which is ascribed to the adsorbed water [21]. However, after chemical treatment two peaks at 531.9 and 533.8 eV can be observed, attributed to the C=O and C–OH groups respectively [50,56]. These signals are in agreement with the FT-IR observations and indicate that the oxygen species are present as functional groups on the surface rather than adsorbed water, as a result of the H_2SO_4 treatment of g- C_3N_4 . The performed Elemental analysis revealed that the C/N atomic ratio noticeably changed only after chemical treatment, increasing from 0.635 up to 0.669 for sample Chem5 (Table 1). The measured nitrogen content significantly decreased suggesting its substitution by –O and/or –OH groups during the oxidation of g- C_3N_4 layers [57,58]. On the contrary, the hydrogen content slightly increased indicating the protonation of the g- C_3N_4 network. The EDS mapping revealed the homogeneous distribution of C, N and O elements for the treated materials as depicted in Fig. S5.

The above results showed that chemical treatment leads to significant changes in the structure and chemical composition of g- C_3N_4 . At first, H_2SO_4 is intercalated within the Bulk g- C_3N_4 during mixing. Then oxidation of g- C_3N_4 occurs as revealed by the intensification of FT-IR peaks relevant to oxygen containing groups ($963\text{ and }1082\text{ cm}^{-1}$), as well as the appearance of C=O and C–OH bonds in the

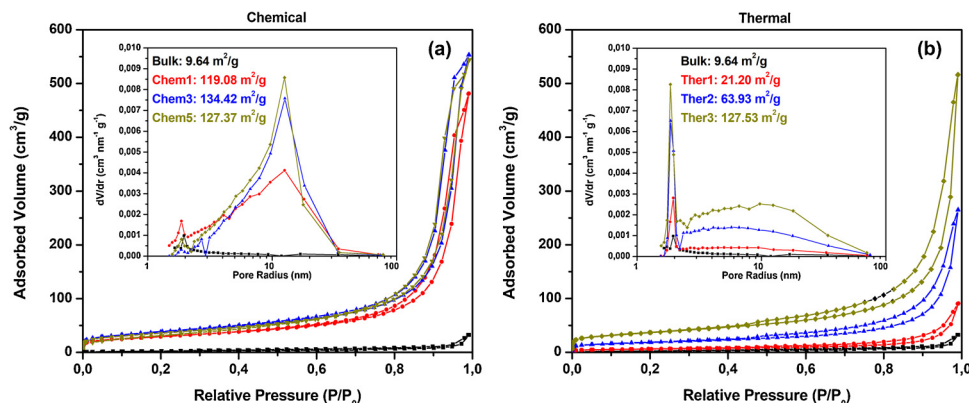


Fig. 2. N_2 adsorption-desorption isotherms and pore size distribution curves of chemically (a) and thermally (b) exfoliated g- C_3N_4 .

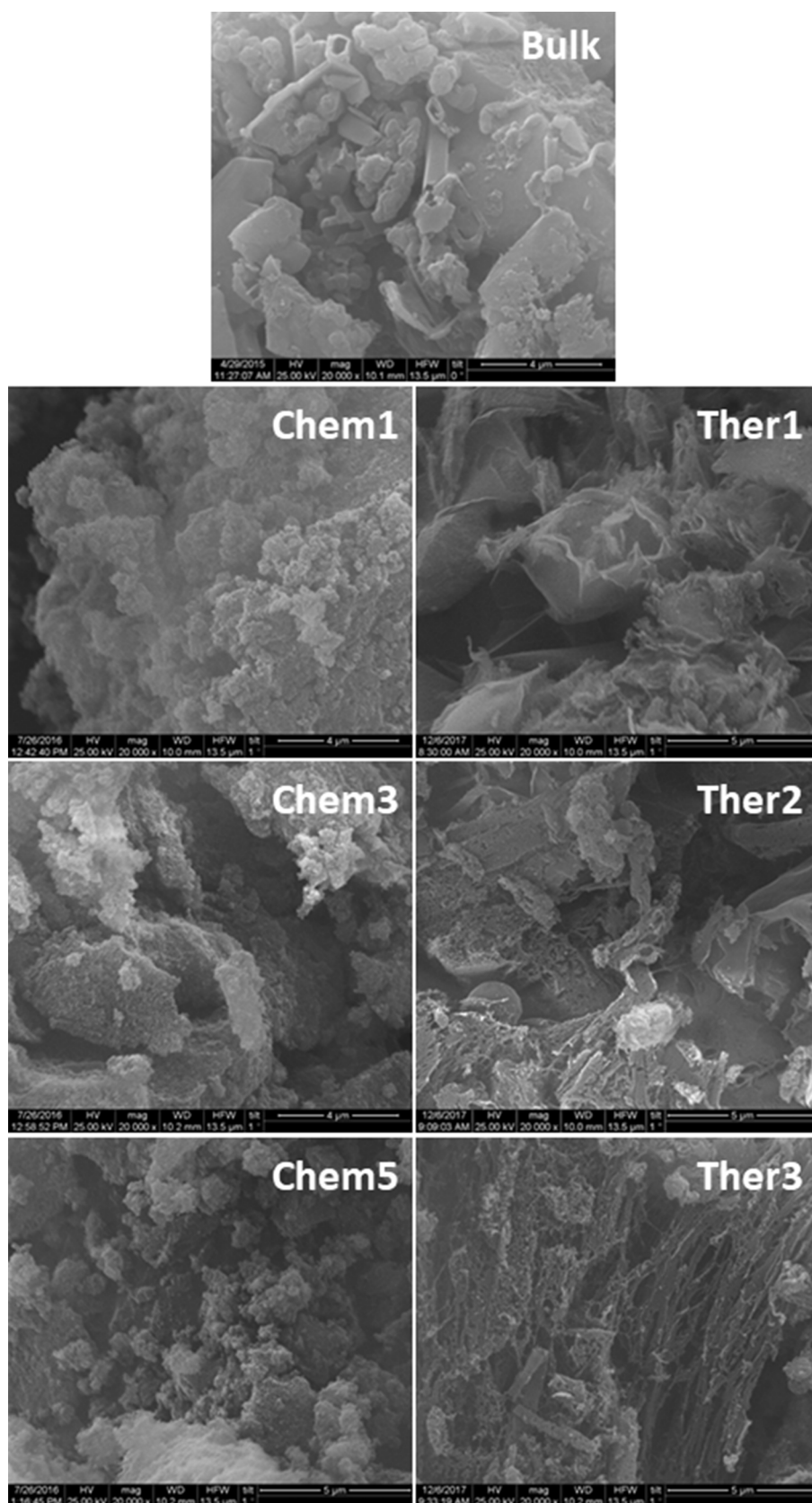


Fig. 3. SEM images of Bulk and exfoliated g-C₃N₄ materials.

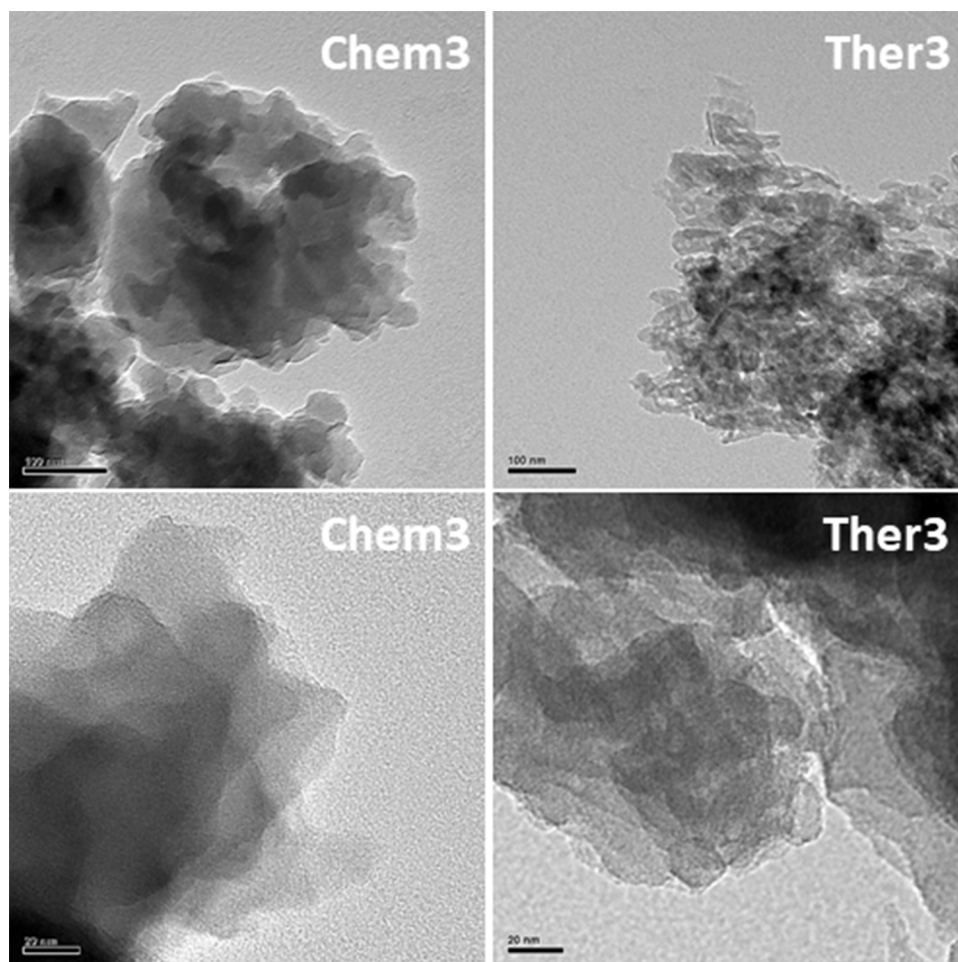


Fig. 4. TEM images of Chem3 and Ther3 samples.

XPS spectra. Next, dissociation of the linking groups and cleavage of g- C_3N_4 network takes place due to the rapid exothermic effect caused by the gradual addition of water. This phenomenon was demonstrated by the appearance of dimelem characteristic FT-IR peak (1602 cm^{-1}), as well as the decrease of the in-plane periodicity according to the XRD results. Also, protonation of the smaller g- C_3N_4 fragments was revealed by the increased (doubled) content of hydrogen, as evidenced by the Elemental analysis measurements. These changes are schematically presented in Fig. 7.

3.4. Light absorbance

The absorption functions $(F^*E)^{1/2} = f(E)$ of the prepared materials are presented in Fig. 8. They were constructed from Kubelka-Munk functions $F(R) = (1 - R)^2/2R$ utilizing the measured diffuse reflectance spectra R of the materials (Fig. S6). The extrapolation of the linear part of the absorption functions permitted the determination of the materials' band gap energy (E_g) [59,60]. The obtained band gap values are presented in Table 1. The E_g of Bulk was 2.63 eV, while significant band gap increase was observed after treatment. The blue-

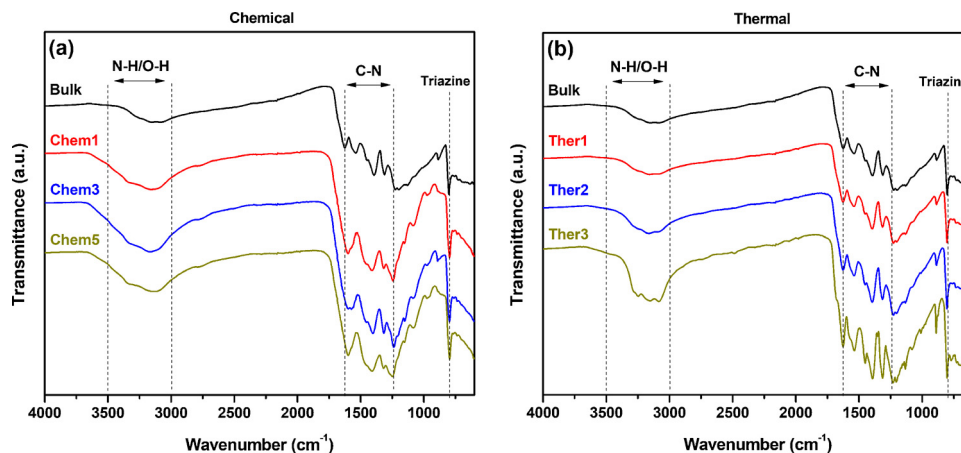


Fig. 5. FT-IR spectra of chemically (a) and thermally (b) exfoliated g- C_3N_4 .

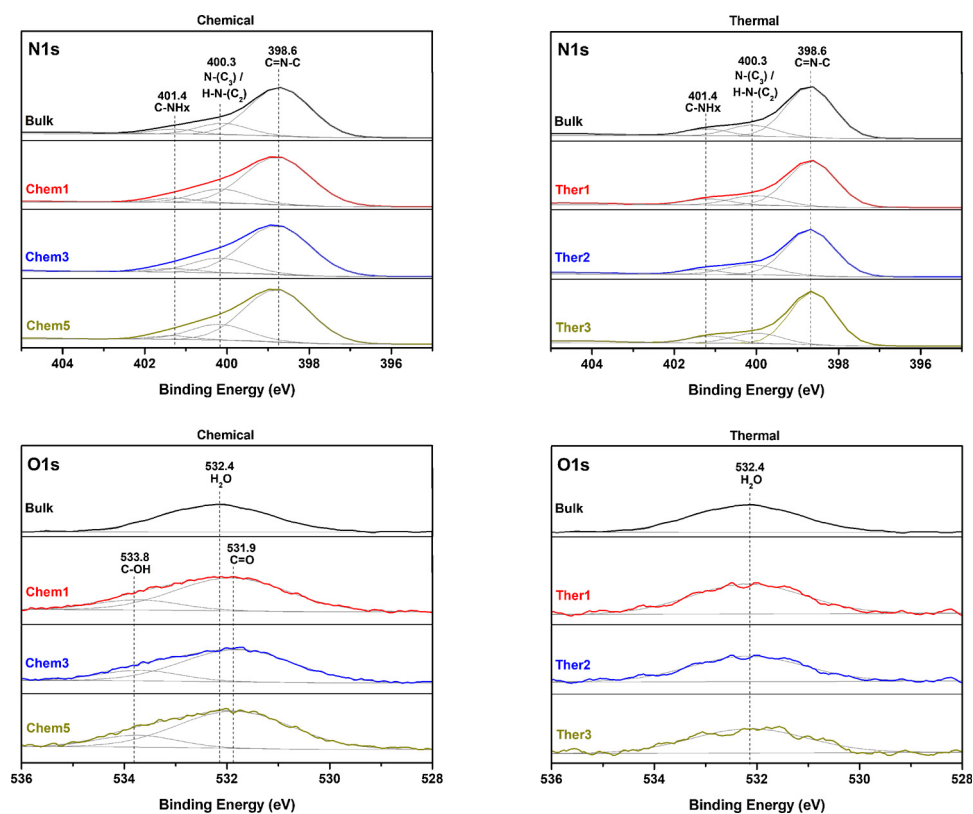


Fig. 6. XPS spectra (N1s and O1s) of chemically (left) and thermally (right) exfoliated g-C₃N₄.

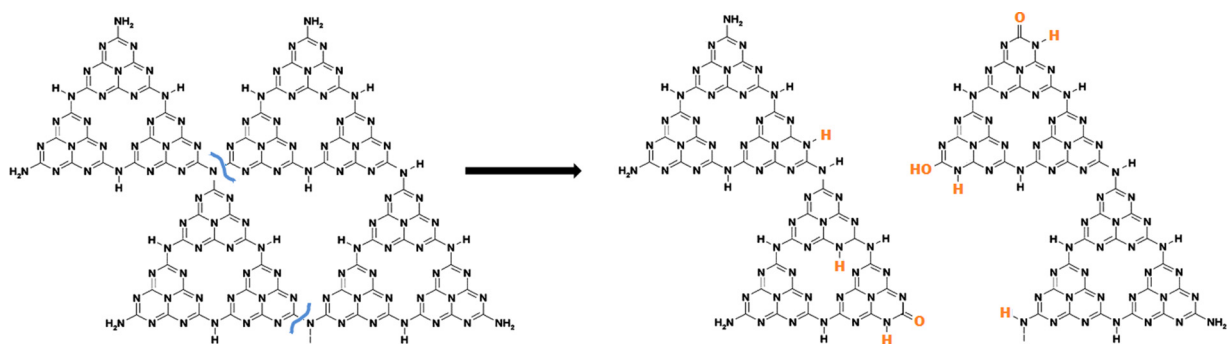


Fig. 7. Schematic illustration of the proposed chemical exfoliation process.

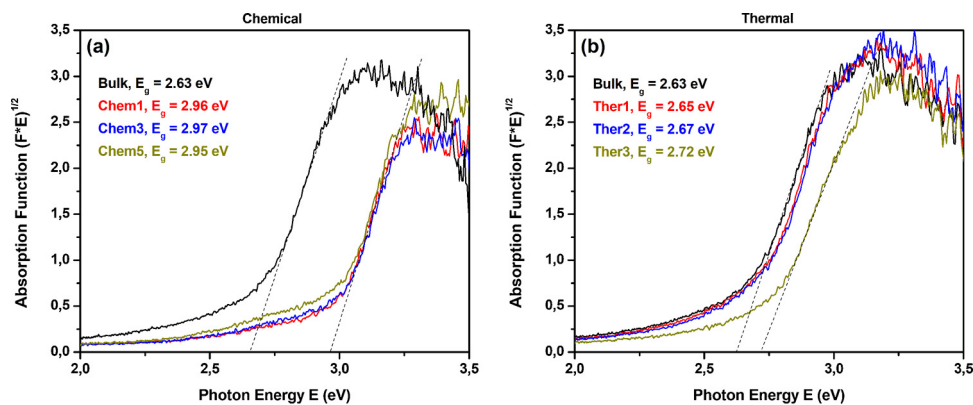


Fig. 8. Plots of $(F \times E)^{1/2}$ vs photon energy of chemically (a) and thermally (b) exfoliated g-C₃N₄.

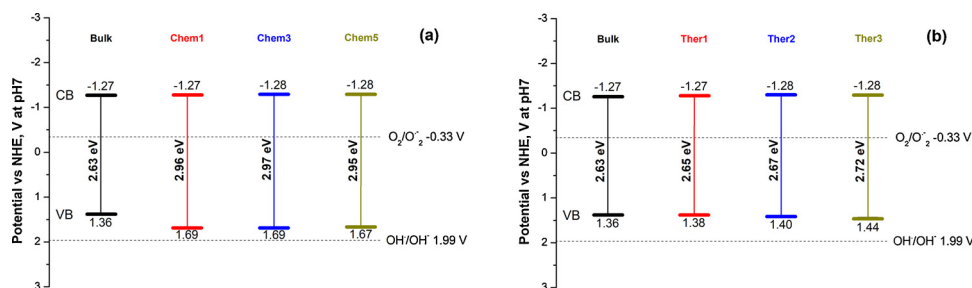


Fig. 9. Band edge potentials of chemically (a) and thermally (a) exfoliated g-C₃N₄.

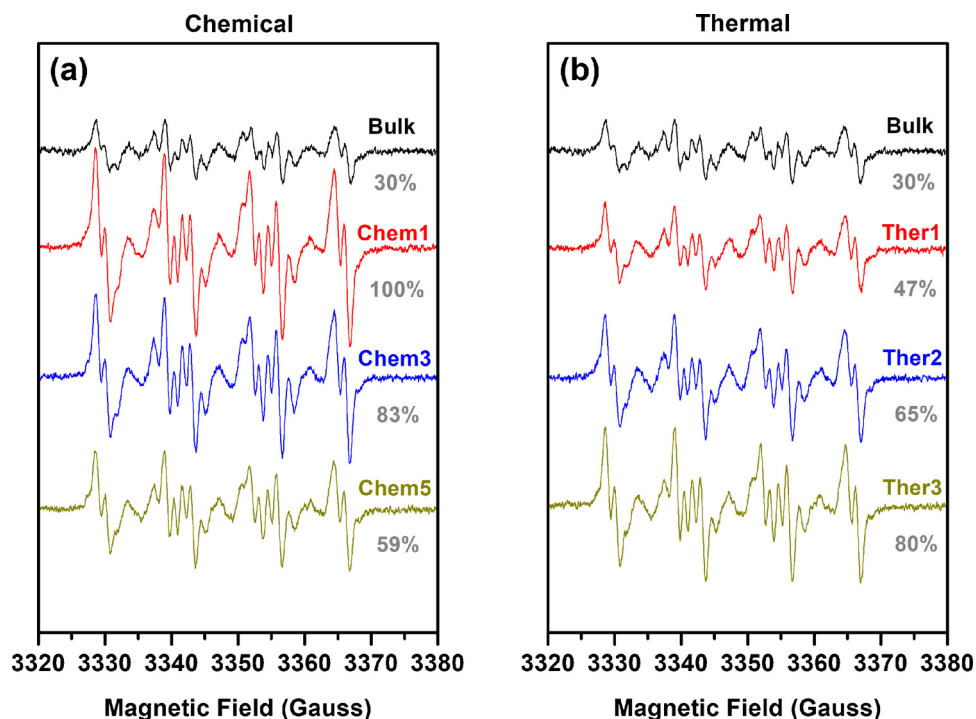


Fig. 10. Detection of radical adducts of DMPO upon visible light irradiation of the chemically (a) and thermally (b) exfoliated g-C₃N₄.

shift can be ascribed to the smaller crystalline size [61] and the quantum confinement effect (QCE) due to the reduced thickness of the stacked layers [20,46]. This feature is more prominent after chemical exfoliation with all samples showing E_g around 2.96 eV, possibly due to the substantial effect of the chemical treatment on the g-C₃N₄ framework, in accordance with the XRD results. The conduction band edge (CB) of the materials obtained via electrochemical measurements (Fig. 9) remained unchanged, while the calculated valence band edge (VB) increased to more positive values. Thus, the high reductive power of the photogenerated electrons is preserved, while the mobility of generated holes increased providing better oxidation efficiency [14]. This outcome indicates that enhanced photocatalytic activity could be expected for the exfoliated g-C₃N₄ materials.

3.5. EPR spectroscopy

The EPR spin-trapping results with DMPO, presented in Fig. 10 and Table S1, clearly indicate that visible light irradiation of g-C₃N₄ induced charge separation in which the CB electrons reacted with dissolved O₂ to form O₂•⁻ [62,63]. After treatment there was a significant increase in the superoxide radical formation. This increase was more prominent for the chemically exfoliated g-C₃N₄ owing to the higher SSA and larger V_p that provides more active sites, with sample Chem1 demonstrating the best behavior. However, this effect seems to be reversed with extended H₂SO₄ treatment. On the other hand, the

thermally exfoliated g-C₃N₄ showed an increasing superoxide radical formation with the process time, with sample Ther3 displaying the best results. Such trend was also observed by the BET and UV-vis analyses.

The measurement of the reactivity of photogenerated electrons showed that the exfoliated materials cause faster chemical reduction of TEMPO to TEMPOH in comparison to Bulk g-C₃N₄ (Fig. 11). Similarly to the spin trapping observations, the rate of TEMPO reduction increases depending on the thermal treatment time but decreases after extensive chemical treatment.

Overall, the EPR results indicated that samples Chem1 and Ther3 are expected to exhibit the best photocatalytic behavior, since they showed the highest superoxide radical formation and reactivity of photogenerated electrons.

3.6. Photocatalytic activity

To demonstrate the photocatalytic activity of the materials in air purification, NO oxidation experiments were performed under visible light irradiation and the results are presented in Figs. 12 and 13. It is immediately apparent that the exfoliated materials provide significantly improved photocatalytic results in comparison with Bulk g-C₃N₄. This could be attributed to the higher SSA which provide more active sites for the redox reactions and the increased V_p which facilitates the transfer of intermediates and final products. After chemical treatment, the materials showed excellent photocatalytic activity,

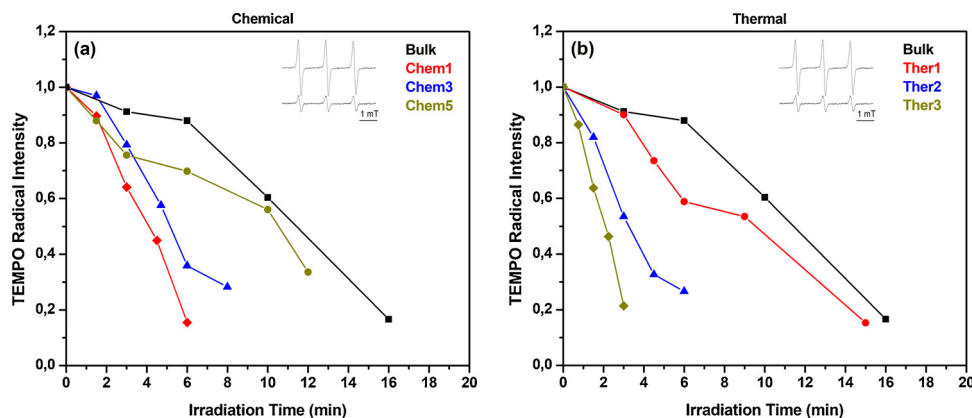
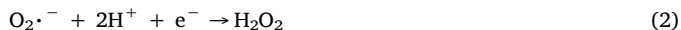


Fig. 11. Dependence of the EPR signal intensity of TEMPO upon irradiation time for chemically (a) and thermally (b) exfoliated g-C₃N₄. The inset shows EPR spectra of TEMPO before and after irradiation in the presence of g-C₃N₄.

reaching up to nine times better (Chem1) NO oxidation than Bulk. The concentration of intermediate toxic NO₂ remained considerably low, hence providing a significantly improved total NO_x removal with sample Chem3 being slightly better. The thermally exfoliated materials showed enhanced NO oxidation gradually increasing with the duration of the thermal treatment, with sample Ther3 exhibiting the best performance reaching four times better activity than Bulk. Despite the fact that sample Ther3 has similar SSA and V_p to the chemically exfoliated g-C₃N₄, its overall photocatalytic activity remained significantly lower. For this reason, the critical parameters governing the activity of the prepared photocatalysts were further sought. Significant differences were observed in the superoxide radical formation, the E_g, the VB edge position and the pore size distribution, with the most favorable values found for the chemically exfoliated g-C₃N₄. Among them, the E_g could not be suggested as a major factor since the enlarged band gap would in principal lead to restricted absorption of visible light. Also, although improved after exfoliation, the VB edge is still less positive than the redox potential of OH⁻/OH• (1.99 eV vs NHE) and therefore the holes cannot oxidize OH⁻ into OH• radicals. Consequently, the pore size distribution and the superoxide radical formation are considered the most critical parameters influencing the photocatalytic performance of the materials. The favorable pore size facilitates the contact between the photocatalyst and the gas pollutant, while the superoxide radicals are involved directly (Eq. (1)) in the NO to NO₃⁻ oxidation [64–66] and indirectly (Eqs. (2), (3)) in the OH• formation [67–69] which participate in the NO_x removal mechanism (Eqs. (4), (5)).



Thus, chemical treatment resulted in exfoliated g-C₃N₄ materials with properties suitable for efficient NO_x removal and stable behavior as shown in Fig. S8, where the activity for five photocatalytic cycles is presented.

4. Conclusions

In conclusion, melamine-derived g-C₃N₄ was successfully exfoliated by chemical and thermal treatment as evidenced by XRD and SEM analyses. Although all treated materials exhibited improved photocatalytic performance in comparison to Bulk g-C₃N₄, important differences were observed between the exfoliated materials prepared with the two methods. It was established that the specific surface area, porosity and band gap energy increased with the duration of thermal treatment. In contrast, the duration of chemical treatment did not have a significant influence on these properties, as high values were obtained even after 1 h of treatment. According to FT-IR and XPS results, the chemical exfoliation led to the cleavage of g-C₃N₄ network and creation of smaller protonated layer fragments. Also, the VB was shifted to more positive values thus further increasing the oxidation potential of the materials. Moreover, the EPR measurements demonstrated that chemical exfoliation results in increased superoxide radical formation. Regarding NO_x removal, the chemically exfoliated g-C₃N₄ showed superior photocatalytic activity under visible light irradiation. This was attributed to the favorable band gap edges, the enhanced formation of superoxide radicals and accelerated transfer of pollutants due to the larger pore volume and specific surface area.

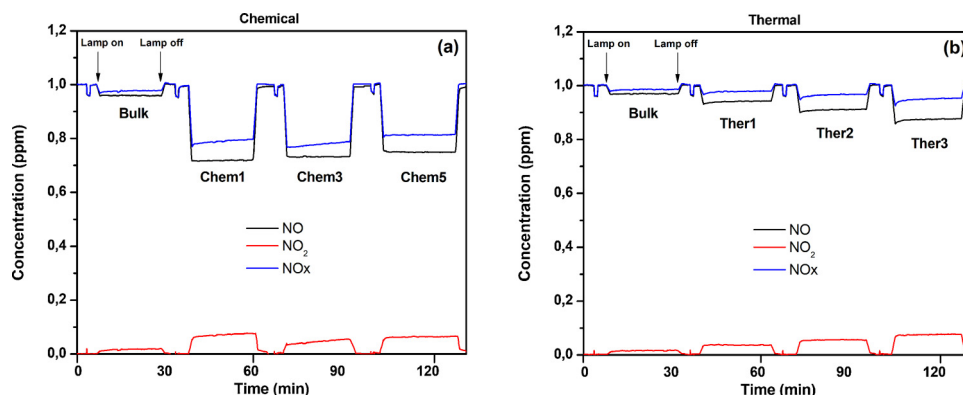


Fig. 12. Experimental concentration curves of chemically (a) and thermally (b) exfoliated g-C₃N₄ under visible light irradiation.

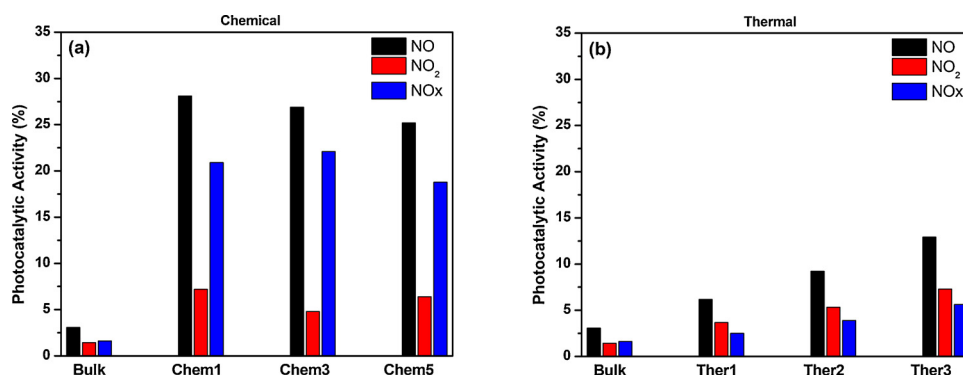


Fig. 13. Photocatalytic activity of chemically (a) and thermally (b) exfoliated g-C₃N₄ under visible light irradiation.

Comparing the two exfoliation methods, thermal treatment offers a facile and inexpensive way of improving the photocatalytic activity of g-C₃N₄, whereas chemical treatment demands multiple steps but leads to excellent NO oxidation and superior NO_x removal. Overall, the exfoliated g-C₃N₄ materials are very promising as they display exceptional results, without the need for complicated heterostructures and/or procedures.

Acknowledgements

The authors appreciate the financial support from GSRT T1EDK-05545 “2D Photostructure” and IKY “2D2D PhotoNOx” projects. The IKY research was funded by the “Strengthening Post-Doctoral Researchers” program from the resources of the EP “Human Resources Development, Education and Lifelong Learning” with Priority Axes 6, 8, 9 and co-funded by the European Social Fund –ESF and the Greek State”.

Appendix A. Supplementary data

Supplementary material related to this article can be found, in the online version, at doi:<https://doi.org/10.1016/j.apcatb.2018.07.078>.

References

- [1] B. Zhao, S.X. Wang, H. Liu, J.Y. Xu, K. Fu, Z. Klimont, J.M. Hao, K.B. He, J. Cofala, M. Amann, NO_x emissions in China: historical trends and future perspective, *Atmos. Chem. Phys.* 13 (2013) 9869–9897.
- [2] K. Skalska, J.S. Miller, S. Ledakowicz, Trends in NO_x abatement: a review, *Sci. Total Environ.* 408 (2010) 3976–3989.
- [3] K.R. Reddy, M. Hassan, V.G. Gomes, Hybrid nanostructures based on titanium dioxide for enhanced photocatalysis, *Appl. Catal. A Gen.* 489 (2015) 1–16.
- [4] X. Li, J.Q. Wen, J.X. Low, Y.P. Fang, J.G. Yu, Design and fabrication of semiconductor photocatalyst for photocatalytic reduction of CO₂ to solar fuel, *Sci. China Mater.* 57 (2014) 70–100.
- [5] X.C. Wang, K. Maeda, A. Thomas, K. Takanabe, G. Xin, J.M. Carlsson, K. Domen, M. Antonietti, A metal-free polymeric photocatalyst for hydrogen production from water under visible light, *Nat. Mater.* 8 (2009) 76–80.
- [6] I. Papailias, T. Giannakopoulou, N. Todorova, D. Demotikali, T. Vaimakis, C. Trapalis, Effect of processing temperature on structure and photocatalytic properties of g-C₃N₄, *Appl. Surf. Sci.* 358 (2015) 278–286.
- [7] S.W. Cao, J.G. Yu, g-C₃N₄-based photocatalysts for hydrogen generation, *J. Phys. Chem. Lett.* 5 (2014) 2101–2107.
- [8] Z.W. Zhao, Y.J. Sun, F. Dong, Graphitic carbon nitride based nanocomposites: a review, *Nanoscale* 7 (2005) 15–37.
- [9] X.C. Wang, S. Blechert, M. Antonietti, Polymeric graphitic carbon nitride for heterogeneous photocatalysis, *ACS Catal.* 2 (2012) 1596–1606.
- [10] T.Y. Ma, S. Dai, M. Jaroniec, S.Z. Qiao, Graphitic carbon nitride nanosheet carbon nanotube three-dimensional porous composites as high-performance oxygen evolution electrocatalysts, *Angew. Chem. Int. Ed.* 53 (2014) 7281–7285.
- [11] S. Hu, L. Ma, J. You, F. Li, Z. Fan, G. Lu, D. Liu, J. Gui, Enhanced visible light photocatalytic performance of g-C₃N₄ photocatalysts co-doped with iron and phosphorus, *Appl. Surf. Sci.* 311 (2014) 164–171.
- [12] J.A. Singh, S.H. Overbury, N.J. Dudley, M.J. Li, G.M. Veith, Gold nanoparticles supported on carbon nitride: influence of surface hydroxyls on low temperature carbon monoxide oxidation, *ACS Catal.* 2 (2012) 1138–1146.
- [13] G. Dong, D.L. Jacobs, L. Zang, C. Wang, Carbon vacancy regulated photoreduction of NO to N₂ over ultrathin g-C₃N₄ nanosheets, *Appl. Catal. B Environ.* 218 (2017) 515–524.
- [14] J. Ding, W. Xu, H. Wan, D. Yuan, C. Chen, L. Wang, G. Guan, W.L. Dai, Nitrogen vacancy engineered graphitic C₃N₄-based polymers for photocatalytic oxidation of aromatic alcohols to aldehydes, *Appl. Catal. B Environ.* 221 (2018) 626–634.
- [15] F. Jiang, T. Yan, H. Chen, A. Sun, C. Xu, X. Wang, A g-C₃N₄-CdS composite catalyst with high visible-light-driven catalytic activity and photostability for methylene blue degradation, *Appl. Surf. Sci.* 295 (2014) 164–172.
- [16] Y.L. Tian, B.B. Chang, J.L. Lu, J. Fu, F.N. Xi, X.P. Dong, Hydrothermal synthesis of graphitic carbon nitride Bi₂WO₆ heterojunctions with enhanced visible light photocatalytic activities, *ACS Appl. Mater. Interfaces* 5 (2013) 7079–7085.
- [17] L. Ge, C.C. Han, J. Liu, Novel visible light-induced g-C₃N₄/Bi₂WO₆ composite photocatalysts for efficient degradation of methyl orange, *Appl. Catal. B Environ.* 108 (2011) 100–107.
- [18] J. Li, E. Liu, Y. Ma, X. Hu, J. Wan, L. Sun, J. Fan, Synthesis of MoS₂/g-C₃N₄ nanosheets as 2D heterojunction photocatalysts with enhanced visible light activity, *Appl. Surf. Sci.* 364 (2016) 694–702.
- [19] J. Xu, L. Zhang, R. Shi, Y. Zhu, Chemical exfoliation of graphitic carbon nitride for efficient heterogeneous photocatalysis, *J. Mater. Chem. A* 1 (2013) 14766–14772.
- [20] J. Tong, L. Zhang, F. Li, K. Wang, L. Han, S. Cao, Rapid and high-yield production of g-C₃N₄ nanosheets via chemical exfoliation for photocatalytic H₂ evolution, *RSC Adv.* 5 (2015) 88149–88153.
- [21] H.J. Li, B.W. Sun, L. Sui, D.J. Qian, M. Chen, Preparation of water-dispersible porous g-C₃N₄ with improved photocatalytic activity by chemical oxidation, *Phys. Chem. Chem. Phys.* 17 (2015) 3309–3315.
- [22] P. Niu, L. Zhang, G. Liu, H.M. Cheng, Graphene-like carbon nitride nanosheets for improved photocatalytic activities, *Adv. Funct. Mater.* 22 (2012) 4763–4770.
- [23] F. Dong, Y. Li, Z. Wang, W.K. Ho, Enhanced visible light photocatalytic activity and oxidation ability of porous graphene-like g-C₃N₄ nanosheets via thermal exfoliation, *Appl. Surf. Sci.* 358 (2015) 393–403.
- [24] Y. Li, M.Q. Wang, S.J. Bao, S. Lu, M. Xu, D. Long, S. Pu, Tuning and thermal exfoliation graphene-like carbon nitride nanosheets for superior photocatalytic activity, *Ceram. Int.* 42 (2016) 18521–18528.
- [25] R. Beranek, (Photo)electrochemical methods for the determination of the band edge positions of TiO₂-based nanomaterials, *Adv. Phys. Chem.* 2011 (2011) 78675920 pages.
- [26] T. Giannakopoulou, I. Papailias, N. Todorova, Nikos Boukos, Y. Liu, J.G. Yu, C. Trapalis, Tailoring the energy band gap and edges’ potentials of g-C₃N₄/TiO₂ composite photocatalysts for NO_x removal, *Chem. Eng. J.* 310 (2017) 571–580.
- [27] C. Baumanis, D.W. Bahnemann, TiO₂ thin film electrodes: correlation between photocatalytic activity and electrochemical properties, *J. Phys. Chem. C* 112 (2008) 19097–19101.
- [28] M. Anpo, M. Che, B. Fubini, E. Garrone, E. Giamello, M.C. Paganini, Generation of superoxide ions at oxide surfaces, *Top. Catal.* 8 (1999) 189–198.
- [29] E. Morra, E. Giamello, M. Chiesa, EPR approaches to heterogeneous catalysis. The chemistry of titanium in heterogeneous catalysts and photocatalysts, *J. Magn. Reson.* 280 (2017) 89–102.
- [30] S. Stoll, A. Schweiger, EasySpin, a comprehensive software package for spectral simulation and analysis in EPR, *J. Magn. Reson.* 178 (2006) 42–55.
- [31] D. Dvoranová, Z. Barbieriková, V. Brezová, Radical Intermediates in Photoinduced Reactions on TiO₂ (An EPR Spin Trapping Study), *Molecules* 19 (2014) 17279–17304.
- [32] ISO/DIS 22197-1, Fine Ceramics (Advanced Ceramics, Advanced Technical Ceramics) - Test Method for Air-purification Performance of Semiconducting Photocatalytic Materials - Part 1: Removal of Nitric Oxide, (2007), pp. 1–11.
- [33] S. Wan, Q. Zhong, M. Ou, S. Zhang, W. Cai, Facial synthesis of sheet-like carbon nitride from preorganized hydrogen bonded supramolecular precursors and its high efficient photocatalytic oxidation of gas-phase NO, *J. Photochem. Photobiol. A Chem.* 340 (2017) 135–145.
- [34] S. Wan, Q. Zhong, M. Ou, S. Zhang, Highly efficient simulated solar-light photocatalytic oxidation of gaseous NO with porous carbon nitride from copolymerization with thymine and mechanistic analysis, *RSC Adv.* 6 (2016) 101208–101215.
- [35] M. Ou, S. Wan, Q. Zhong, S. Zhang, Y. Wang, Single Pt atoms deposition on g-C₃N₄ nanosheets for photocatalytic H₂ evolution or NO oxidation under visible light, *Int. J. Hydrogen Energy* 42 (2017) 27043–27054.

- [36] J. Chen, S. Shen, P. Guo, P. Wu, L. Guo, Spatial engineering of photo-active sites on g-C₃N₄ for efficient solar hydrogen generation, *J. Mater. Chem. A* 2 (2014) 4605–4612.
- [37] Y. Shiraishi, S. Kanazawa, Y. Sugano, D. Tsukamoto, H. Sakamoto, S. Ichikawa, T. Hirai, Highly selective production of hydrogen peroxide on graphitic carbon nitride (g-C₃N₄) photocatalyst activated by visible light, *ACS Catal.* 4 (2014) 774–780.
- [38] H.J. Yan, Y. Chen, S.M. Xu, Synthesis of graphitic carbon nitride by directly heating sulfuric acid treated melamine for enhanced photocatalytic H₂ production from water under visible light, *Int. J. Hydrogen Energy* 37 (2012) 125–133.
- [39] W.K. Ho, Z. Zhang, M. Xu, X. Zhang, X. Wang, Y. Huang, Enhanced visible-light-driven photocatalytic removal of NO: effect on layer distortion on g-C₃N₄ by H₂ heating, *Appl. Catal. B Environ.* 179 (2015) 106–112.
- [40] H. Zhao, X.L. Chen, C. Jia, T. Zhou, X. Qu, J. Jian, Y. Xu, T. Zhou, A facile mechanochemical way to prepare g-C₃N₄, *Mater. Sci. Eng. B* 122 (2005) 90–93.
- [41] H. Zhao, H. Yu, X. Quan, S. Chen, Y. Zhang, H. Zhao, H. Wang, Fabrication of atomic single layer graphitic-C₃N₄ and its high performance of photocatalytic disinfection under visible light irradiation, *Appl. Catal. B Environ.* 152–153 (2014) 46–50.
- [42] K. Wang, Q. Li, B. Liu, B. Cheng, W. Ho, J.G. Yu, Sulfur-doped g-C₃N₄ with enhanced photocatalytic CO₂-reduction performance, *Appl. Catal. B Environ.* 176–177 (2015) 44–52.
- [43] Z. Zhao, Y. Sun, Q. Luo, F. Dong, H. Li, W.K. Ho, Mass-controlled direct synthesis of graphene-like carbon nitride nanosheets with exceptional high visible light activity, *Less is Better, Sci. Rep.* 5 (2015) 14643.
- [44] X. Song, Q. Yang, X. Jiang, M. Yin, L. Zhou, Porous graphitic carbon nitride nanosheets prepared under self-producing atmosphere for highly improved photocatalytic activity, *Appl. Catal. B Environ.* 217 (2017) 322–330.
- [45] C.J. Wang, Z.W. Zhao, B. Luo, M. Fu, F. Dong, Tuning the morphological structure and photocatalytic activity of nitrogen doped (BiO)₂CO₃ by the hydrothermal temperature, *J. Nanomater.* 2014 (2014) 192797.
- [46] X. Yuan, C. Zhou, Y. Jin, Q. Jing, Y. Yang, X. Shen, Q. Tang, Y. Mua, A.K. Du, Facile synthesis of 3D porous thermally exfoliated g-C₃N₄ nanosheet with enhanced photocatalytic degradation of organic dye, *J. Colloid Interface Sci.* 468 (2016) 211–219.
- [47] M.J. Boidys, J.O. Muller, M. Antonietti, A. Thomas, Ionothermal synthesis of crystalline, condensed graphitic carbon nitride, *Chem. Eur. J.* 14 (2008) 8177–8182.
- [48] B. Zhu, P. Xia, W.K. Ho, J.G. Yu, Isoelectric point and adsorption activity of porous g-C₃N₄, *Appl. Surf. Sci.* 344 (2015) 188–195.
- [49] F. Dong, L.W. Wu, Y.J. Sun, M. Fu, Z.B. Wu, S.C. Lee, Efficient synthesis of polymeric g-C₃N₄ layered materials as novel efficient visible light driven photocatalysts, *J. Mater. Chem.* 21 (2011) 15171–15174.
- [50] W.J. Ong, L.L. Tan, S.P. Chai, S.T. Yong, A.R. Mohamed, Surface charge modification via protonation of graphitic carbon nitride (g-C₃N₄) for electrostatic self-assembly construction of 2D/2D reduced graphene oxide (rGO)/g-C₃N₄ nanostructures toward enhanced photocatalytic reduction of carbon dioxide to methane, *Nano Energy* 13 (2015) 757–770.
- [51] Y. Cao, Q. Lia, W. Wang, Construction of a crossed-layer-structure MoS₂/g-C₃N₄ heterojunction with enhanced photocatalytic performance, *RSC Adv.* 7 (2017) 6131–6139.
- [52] A.I. Finkel'shtein, N.V. Spiridonova, Chemical properties and molecular structure of derivatives of sym-heptazine [1,3,4,6,7,9,9b-heptaazaphenylene, tri-1,3,5-triazine], *Russ. Chem. Rev.* 33 (1964) 400–405.
- [53] X. Wei, Y. Qiu, W. Duan, Z. Liu, Cathodic and anodic photocurrents generation from melam and its derivatives, *RSC Adv.* 5 (2015) 26675–26679.
- [54] X. Yang, F. Qian, G. Zou, M. Li, J. Lu, Y. Li, M. Bao, Facile fabrication of acidified g-C₃N₄/g-C₃N₄ hybrids with enhanced photocatalysis performance under visible light irradiation, *Appl. Catal. B Environ.* 193 (2016) 22–35.
- [55] C. Ye, J.X. Li, Z.J. Li, X.B. Li, X.B. Fan, L.P. Zhang, B. Chen, C.H. Tung, L.Z. Wu, Enhanced driving force and charge separation efficiency of protonated g-C₃N₄ for photocatalytic O₂ evolution, *ACS Catal.* 5 (2015) 6973–6979.
- [56] Y. Yang, L. Geng, Y. Guo, J. Meng, Y. Guo, Easy dispersion and excellent visible-light photocatalytic activity of the ultrathin urea-derived g-C₃N₄ nanosheets, *Appl. Surf. Sci.* 425 (2017) 535–546.
- [57] X. Guo, Y. Wang, F. Wu, Y. Ni, S. Kokot, Preparation of protonated, two-dimensional graphitic carbon nitride nanosheets by exfoliation, and their application as a fluorescent probe for trace analysis of copper(II), *Microchim. Acta* 183 (2016) 773–780.
- [58] Z. Yang, K. Hu, X. Meng, Q. Tao, J. Dong, B. Liu, Q. Lu, H. Zhang, B. Sundqvist, P. Zhu, M. Yao, B. Liu, Tuning the band gap and the nitrogen content in carbon nitride materials by high temperature treatment at high pressure, *Carbon* 130 (2018) 170–177.
- [59] A.B. Murphy, Band-gap determination from diffuse reflectance measurements of semiconductor films, and application to photoelectrochemical water-splitting, *Sol. Energy Mater. Sol. Cells* 91 (2007).
- [60] T. Giannakopoulou, N. Todorova, G. Romanos, T. Vaimakis, R. Dillert, D. Bahnemann, C. Trapalis, Composite hydroxyapatite/TiO₂ materials for photocatalytic oxidation of NOx, *Mater. Sci. Eng. B* 177 (2012) 1046–1052.
- [61] W.B. Luo, S.L. Chou, J.Z. Wang, Y.C. Zhai, H.K. Liu, A metal-free, free-standing, mesoporous graphene@g-C₃N₄ composite air electrode for high-energy lithium oxygen batteries, *Small* 11 (2015) 2817–2824.
- [62] Y. Nosaka, A.Y. Nosaka, Identification and roles of the active species generated on various photocatalysts, in: P. Pichat (Ed.), *Photocatalysis and Water Purification: From Fundamentals to Recent Applications*, Wiley-VCH, Weinheim, Germany, 2013, pp. 3–24.
- [63] V. Brezová, S. Gabčová, D. Dvoranová, A. Staško, Reactive oxygen species produced upon photoexcitation of sunscreens containing titanium dioxide (An EPR study), *J. Photochem. Photobiol. B Biol.* 79 (2005) 121–134.
- [64] F. Dong, Z. Zhao, Y. Sun, Y. Zhang, S. Yan, Z. Wu, An advanced semimetal-organic Bi spheres/g-C₃N₄ nanohybrid with SPR enhanced visible-light photocatalytic performance for NO purification, *Environ. Sci. Technol.* 49 (2015) 12432–12440.
- [65] Q. Zhang, Y. Huang, S. Peng, Y. Zhang, Z. Shen, J. Cao, W.K. Ho, S.C. Lee, D.Y.H. Pui, Perovskite LaFeO₃-SrTiO₃ composite for synergistically enhanced NO removal under visible light excitation, *Appl. Catal. B Environ.* 204 (2017) 346–357.
- [66] Q. Zhang, Y. Huang, L. Xu, J. Cao, W.K. Ho, S.C. Lee, Visible-light-active plasmonic Ag-SrTiO₃ nanocomposites for the degradation of NO in air with high selectivity, *ACS Appl. Mater. Interfaces* 8 (2016) 4165–4174.
- [67] M. Ou, S. Wan, Q. Zhong, S. Zhang, Y. Song, L. Guo, W. Cai, Y. Xu, Hierarchical Z-scheme photocatalyst of g-C₃N₄@Ag/BiVO₄ (040) with enhanced visible-light-induced photocatalytic oxidation performance, *Appl. Catal. B Environ.* 221 (2018) 97–107.
- [68] F. Dong, Q. Li, Y. Sun, W.K. Ho, Noble metal-like behavior of plasmonic Bi particles as a cocatalyst deposited on (BiO)₂CO₃ microspheres for efficient visible light photocatalysis, *ACS Catal.* 4 (2014) 4341–4350.
- [69] S. Wan, M. Ou, Q. Zhong, S. Zhang, Z-scheme CaIn₂S₄/Ag₃PO₄ nanocomposite with superior photocatalytic NO removal performance: fabrication, characterization and mechanistic study, *New J. Chem.* 42 (2018) 318–326.